

Origin of the Golden Mass of Galaxies and Black Holes

Avishai Dekel^{1,2}, Sharon Lapiner¹, and Yohan Dubois³

¹ Racah Institute of Physics, The Hebrew University, Jerusalem 91904 Israel

e-mail: dekel@huji.ac.il

² SCIPP, University of California, Santa Cruz, CA 95064, USA

³ Institut d'Astrophysique, 98 bis Boulevard Arago, 75014 Paris, France

April 19, 2019

ABSTRACT

Aims. We address the origin of the golden mass and time for galaxy formation and the onset of rapid black-hole growth. The preferred dark-halo mass of $\sim 10^{12} M_{\odot}$ is translated to a characteristic epoch, $z \sim 2$, at which the typical forming halos have a comparable mass.

Methods. We put together a coherent picture based on existing and new simple analytic modeling and cosmological simulations.

Results. We describe how the golden mass arises from two physical mechanisms that suppress gas supply and star formation below and above the golden mass, supernova feedback and virial shock heating of the circum-galactic medium (CGM), respectively. Cosmological simulations reveal that these mechanisms are responsible for a similar favored mass for the dramatic events of gaseous compaction into compact star-forming “blue nuggets”, caused by mergers, counter-rotating streams or other mechanisms. This triggers inside-out quenching of star formation, to be maintained by the hot CGM, leading to today’s passive early-type galaxies. The blue-nugget phase is responsible for transitions in the galaxy structural, kinematic and compositional properties, e.g., from dark-matter to baryon central dominance and from prolate to oblate shape. The growth of the central black hole is suppressed by supernova feedback below the critical mass, and is free to grow once the halo is massive enough to lock the supernova ejecta by its deep potential well and the hot CGM. A compaction near the golden mass makes the black hole sink to the galactic center and triggers a rapid black-hole growth. This ignites feedback by the Active Galactic Nucleus that helps keeping the CGM hot and maintaining long-term quenching.

Key words. black holes — dark matter — galaxies: evolution — galaxies: formation — galaxies: halos — galaxies: mergers

1. Introduction

The stellar-to-halo mass ratio in galaxies of a given dark-matter halo mass, M_s/M_v , can be interpreted as the efficiency of galaxy formation in such halos. This ratio has been derived by abundance matching of observed galaxies and simulated LCDM halos (Moster et al. 2010; Behroozi et al. 2013, 2018). Figure 1 reveals a robust shape as a function of halo mass, with only little redshift dependence in the redshift range $z=0-4$. It shows a peak of efficiency near a halo virial mass $M_v \sim 10^{12} M_{\odot}$, declining on both sides toward lower and higher masses, indicating the operation of mechanisms that suppress star formation in the two zones below and above the critical mass.

A complementary fundamental observational input is the cosmological evolution of star-formation rate (SFR) density (Madau & Dickinson 2014), shown in Fig. 2. It rises continuously from $z \sim 10$ to $z \sim 2$, where it reaches a peak, followed by a steep decline after $z \sim 1$ till the present. We argue that this critical time, at $z \sim 2-1$, reflects the same critical mass scale that is indicated by the stellar-to-halo ratio. This is because, as obtained from the Press-Schechter formalism (Press & Schechter 1974, PS) and confirmed in cosmological simulations, the typical halos that form at $z \sim 1-2$ are of $10^{11-12} M_{\odot}$, and this typical halo mass is very steeply rising with time.

The density of accretion-rate into halos is declining with time at all epochs, reflecting the expansion of the Universe and the evolution of the halo population. This can be derived from the average specific accretion rate, which in the Einstein-deSitter regime (at $z > 1$) is $\dot{M}/M \propto (1+z)^{5/2}$ (Dekel et al. 2013), convolved with the number density of halos based on the Press-

Schechter formalism. The quoted accretion rate emerges in a simple way from its invariance with respect to the “time” variable $(1+z)$, the inverse of the growing mode of linear fluctuations.

The rise in time of the SFR density prior to the peak at $z \sim 2$, despite the decline in accretion rate, is obtained by the suppression of galaxy formation in low-mass halos that are of the Press-Schechter mass at those high redshifts (Bouché et al. 2010). The drop in SFR density with time at low redshifts, while it qualitatively follows the basic decline in the accretion rate, is significantly steeper, indicating high mass quenching when the Press-Schechter mass is high. Thus, the rise and fall of the SFR density with time is largely determined by the same quenching mechanisms that operate at low and high mass scales and generate the peak in M_s/M_v . The peak epoch of SFR density can thus be interpreted as a manifestation of the critical mass scale for peak efficiency of galaxy formation, which we address here.

The golden mass marks a general bimodality about $M_s \sim 10^{10.5} M_{\odot}$ in many galaxy properties, as summarized in Dekel & Birnboim (2006, hereafter DB06). This includes the characteristics of star formation, morphology, kinematics and composition. DB06 highlighted the key role played by the virial shock heating of the Circum-Galactic Medium (CGM), valid in halos above the critical mass, in generating the bimodality. This will be summarized below (§3) as one of the fundamental process responsible for the golden scale, to be integrated with another basic process, supernova (SN) feedback, which dominates below the critical mass (§2).

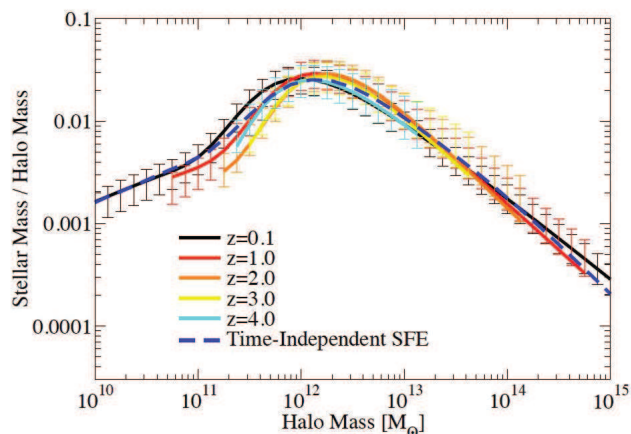


Fig. 1. The efficiency of galaxy formation, represented by the ratio of stellar-to-halo mass, versus halo mass, as derived from observations by abundance matching to LCDM dark-matter halos (Behroozi et al. 2013). Quenching at low masses and at high masses define a peak near a golden mass of $M_v \sim 10^{12} M_\odot$, roughly the same at all redshifts in the range $z=0-4$ (and at higher redshifts). One should mention that AGN are preferentially detected above the golden mass (Förster Schreiber et al. 2018, see the right panel of Fig. 10 below).

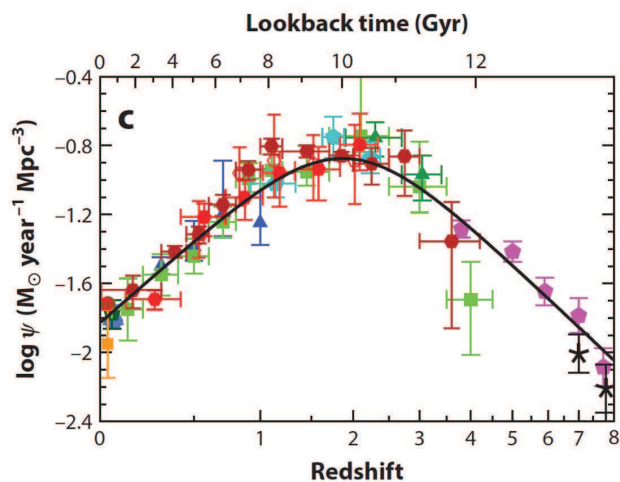


Fig. 2. The star-formation-rate density ψ as a function of redshift (Madau & Dickinson 2014), showing a characteristic epoch for galaxy formation, near $z \sim 2$. This peak reflects the golden mass for galaxy-formation efficiency from Fig. 1, convolved with the fact that the typical mass for forming halos, as evaluated by the Press-Schechter formalism, is comparable to the golden mass at $z \sim 2$. The peak in time is thus a result of low-mass quenching at high redshifts, and of the natural decline of specific accretion rate with time aided by high-mass quenching at low redshifts.

Also pointing to the same golden mass is the fact that Active Galactic Nuclei (AGN) are observed to dominate the emission lines in galaxies above a threshold mass, roughly $M_s \geq 10^{10} M_\odot$, corresponding to $M_v \geq 10^{12} M_\odot$ (Kauffmann et al. 2003; Vitale et al. 2013). A similar threshold mass is observed for AGN-driven outflows at high redshifts (Förster Schreiber et al. 2018). There are indeed preliminary indications that the masses of black holes below $10^6 M_\odot$ fall short of the standard linear relation between black-hole mass and its host bulge mass (Kormendy & Ho 2013; Reines & Volonteri 2015). These indicate that black-hole growth is suppressed in the low-mass zone and it becomes rapid in the high-mass zone, which also implies that AGN feedback is not relevant in low-mass galaxies while

it may contribute to the quenching of high-mass galaxies. There seems to be no feature of black-hole physics that may hint to the origin of such a mass threshold in the black-hole abundance, so one may suspect that it arises from the cross-talk between the black hole and other physical processes in the host galaxy that control the gas supply to the black hole. Understanding the origin of this interplay between galaxy and black-hole evolution is a major goal of galaxy formation, which we attempt to address here.

Both simulations (Zolotov et al. 2015; Tacchella et al. 2016a,b) and observations (Barro et al. 2013; van Dokkum et al. 2015; Barro et al. 2017a) reveal a drastic sequence of events that typically occur in galaxies when they are near the same critical mass (Tomassetti et al. 2016; Huertas-Company et al. 2018). The galaxies undergo dramatic gaseous *compactions* into compact star-forming “blue nuggets”. The major compaction events trigger inside-out quenching of star formation, which is maintained by the hot CGM, leading to today’s passive elliptical galaxies. The blue-nugget phase is responsible for drastic transitions in the main galaxy structural, kinematic and compositional properties (Dekel et al. 2019, in prep.), for example a transition from dark-matter to baryon dominance in the galaxy center.

Here we address the interplay between supernova feedback, CGM heating and wet compaction in generating the golden scale for galaxy formation and activating rapid black-hole growth. We propose that the supernova feedback and the hot CGM define the zones of low-mass and high-mass quenching, as well as the critical mass for efficient compaction between the supernova zone and the hot-CGM zone. In turn, the compaction event causes the transitions in galaxy properties at this mass scale. In particular, it boosts the black hole growth, which then, through AGN feedback, helps the hot CGM maintain the quenching of star formation above this critical mass.

In §2 we revisit the scale arising from supernova feedback, and in §3 the scale associated with a hot CGM. In §4 we summarize the event of wet compaction and its characteristic scale. In §5 we address the quenching mechanism above the critical mass. In §6 we show how the interplay between the above processes and black-hole growth imprints the golden mass in the black-hole and AGN population. In §7 we conclude our findings.

2. The Supernova-Feedback Scale

An upper limit for the dark-matter halo mass (actually its virial velocity) within which supernova feedback can be effective in heating or ejecting the gas and thus suppressing the SFR can be estimated in a simple but robust way using the standard theory for supernova bubbles (e.g. Dekel & Silk 1986). The energy deposited in the ISM by supernovae that arise from a stellar mass M_s is estimated to be

$$E_{\text{SN}} \sim M_s V_{\text{SN}}^2, \quad V_{\text{SN}} \sim 120 \text{ km s}^{-1}. \quad (1)$$

The derivation involves the ratio of two timescales, a cooling time and a dynamical time, which turns out to be roughly constant. These are the duration of the adiabatic phase of the supernova bubble in which it can deposit energy in the ISM before it cools radiatively, and the timescale associated with star formation that is roughly proportional to the dynamical timescale in the star-forming region.

For the supernova energy to heat or eject most of the gas of mass M_g that has accreted into the galaxy it should be comparable to the binding energy of this gas in the dark-matter halo

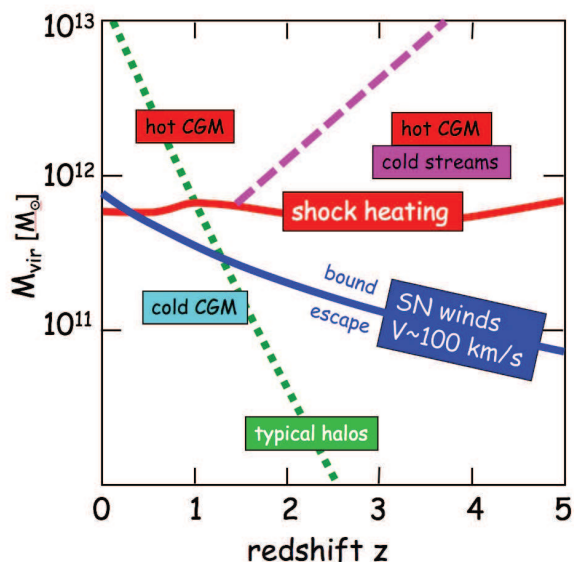


Fig. 3. The characteristic halo masses as a function of redshift. The blue curve marks the upper limit for effective supernova feedback based on Dekel & Silk (1986) (§2). The red curve denotes the threshold for virial shock heating of the CGM based on Dekel & Birnboim (2006) (§3), with the dashed magenta line representing the upper limit for penetrating cold streams. The green short-dash curve refers to the Press-Schechter mass, the typical mass of forming halos. The left portion of the red curve at $z < 2$, combined with the dashed magenta curve at $z > 2$, mark the upper limit for star-forming galaxies. The three masses roughly coincide at $z \sim 1-2$, defining the peak epoch and mass of star formation.

potential well,

$$E_{\text{CGM}} \sim M_g V_v^2, \quad V_v^2 = \frac{GM_v}{R_v}, \quad (2)$$

where M_v and R_v are the halo virial mass and radius, V_v is the halo virial velocity, and V_v^2 characterizes the halo potential well. At the peak of star-formation efficiency, if a large fraction of the gas accreted into the halo turned into stars with little ejection, one has $M_s \sim M_g$. By comparing eq. (1) to eq. (2), this yields a critical upper limit for the virial velocity of a halo in which supernova feedback can be effective,

$$V_v \sim V_{\text{SN}} \sim 120 \text{ km s}^{-1}. \quad (3)$$

Using the standard virial relation, this corresponds to $M_v \sim 10^{11.7} M_\odot$ at $z=0$, and it roughly scales as $(1+z)^{-3/2}$ in the EdS regime (e.g. Dekel & Birnboim 2006, Appendix A2). In haloes above this mass, the potential well is too deep for the supernova-driven winds to escape or for a large fraction of the gas to heat up. This mass scale roughly coincides with the observed peak of star-formation efficiency.

Figure 3 illustrates the critical halo mass corresponding to $V_v = V_{\text{SN}}$ as a function of redshift. Gradually rising with time, it coincides at $z \sim 1-2$ with the steeply-rising Press-Schechter mass that characterizes the typical mass for haloes at a given time.

This simple energetics of supernova feedback can also be used to predict the slope of the stellar-to-halo mass relation in the supernova zone below the critical mass. When $V_v < V_{\text{SN}}$, the shallow potential well allows significant gas ejection, namely $M_s \ll M_g$. The gas mass that has been accreted into the halo is assumed to be roughly proportional to the halo mass, $M_g \propto M_v$. Comparing eq. (1) and eq. (2) then yields (Dekel & Woo 2003)

$$\frac{M_s}{M_v} \propto V_v^2 \propto M_v^{2/3}. \quad (4)$$

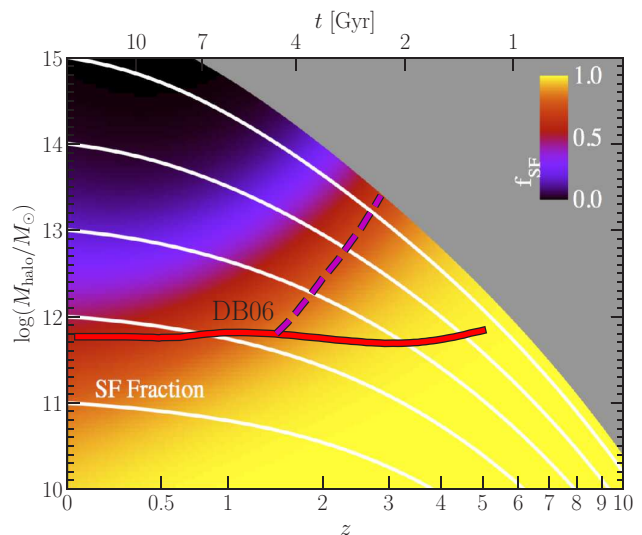


Fig. 4. The fraction of star-forming galaxies as a function of halo mass and redshift, as derived from observed galaxies using abundance matching to LCDM halos (based on Behroozi 2016). The transition from dominance by star-forming versus quenched galaxies (dark red area) matches the theoretical predictions (red and magenta curves), the maximum mass indicated by the curves in Fig. 3 (based on Dekel & Birnboim 2006).

This indeed resembles the slope deduced from observations via abundance matching in the supernova zone (Fig. 1). Note that in the vicinity of the critical potential well, $V_v \sim V_{\text{SN}}$, the assumption of no ejection automatically implies a flat peak, $M_s/M_v \sim \text{const}$.

Similar arguments (Dekel & Woo 2003) lead to the scaling relations of surface brightness with mass in the supernova, dwarf zone, $\mu \propto M_s^{3/5}$, as well as the metallicity with mass, $Z \propto M_s^{2/5}$, and circular velocity with mass, $V \propto M_s^{1/5}$. These simple arguments predict the flattening off of the surface brightness and metallicity relations near the critical mass, and the convergence to the standard Tully-Fisher relation of $V \propto M_s^{1/4}$ there.

Supernova feedback indeed plays a major role in galaxy evolution in the supernova zone, below the golden mass. For example, it can explain the formation of flat cores in dark-matter halos by repeating episodes of star formation and supernovae (Dekel & Silk 1986; Dekel & Woo 2003; Pontzen & Governato 2012; freundlich et al. 2019), the low surface brightness of dwarf galaxies including the recently discovered ultra-diffuse galaxies (Dutton et al. 2016; Di Cintio et al. 2017; Jiang et al. 2018), the missing dwarfs in the local Group (Zolotov et al. 2012; Garrison-Kimmel et al. 2013), and the Kennicutt-Schmidt relation between the global SFR density and gas density (Silk 1997; Ostriker & Shetty 2011; Dekel et al. 2019).

3. The Hot-CGM Scale

The other characteristic scale is the upper limit for the halo mass within which efficient cold inflow can supply gas for star formation (Rees & Ostriker 1977; Silk 1977; Binney 1977). It is obtained by comparing the gas radiative cooling time to the relevant dynamical time for gas inflow. The key question is whether the shock that forms at the halo virial radius, behind which the gas heats to the virial temperature, can be supported against gravitational collapse. For the post-shock gas to be able to sustain the pressure that supports the shock against gravity, its cooling

time has to be longer than the dynamical time for gas compression behind the shock, which is comparable to the halo crossing time, R_v/V_v (Birnboim & Dekel 2003; Dekel & Birnboim 2006). Since the cooling time is an increasing function of halo mass, a shock-stability analysis reveals a threshold mass for a hot CGM on the order of

$$M_v \sim 10^{11.7} M_\odot, \quad (5)$$

roughly independent of redshift in the range $z = 0-3$, with an uncertainty of a factor of a few due to the uncertainty in metallicity and the location within the halo where the shock stability is evaluated. This analysis has been supported by idealized spherical simulations.

Figure 3 shows the predicted critical halo mass for virial shock heating as a function of redshift, based on Dekel & Birnboim (2006, Fig. 7). Below the critical curve one expects the cosmological inflow to be all cold, at $T \sim 10^4$ K, efficiently feeding the galaxy and allowing high SFR. Above the curve one expects the CGM to be shock heated to the virial temperature, thus suppressing the cold gas supply into the galaxy, and maintaining long-term quenching.

At $z \geq 2$, above the shock-heating curve and below the dashed curve, narrow cold streams are expected to penetrate through the otherwise hot CGM and supply gas for efficient star formation even in haloes above the critical mass for shock heating. These predictions, based on an analytic study of virial shock stability and supporting idealized spherical simulations, have been confirmed in cosmological simulations (Kereš et al. 2005; Ocvirk et al. 2008; Nelson et al. 2013, 2016, Fig. xxx).

These predictions, as summarized in Fig. 3, have been confirmed observationally. Figure 4 shows the fraction of star-forming galaxies among the general population of galaxies in the plane of halo mass versus redshift, similar to the plane in Fig. 3. This is based on abundance matching of galaxies to dark-matter haloes in a LCDM cosmology (Behroozi et al. 2018). The transition from low to high SF fraction, marked by the red color, matches the predicted critical curves marking the upper limits for cold gas supply in Fig. 3.

For long-term quenching, the CGM has to be kept hot. This can be caused by gravitational heating due to accreting mass (Dekel & Birnboim 2008), or by AGN feedback (e.g. Croton et al. 2006; Cattaneo & Teyssier 2007; Dubois et al. 2011), see §5 and §6.

4. Wet Compaction to a Blue Nugget

Cosmological simulations show that most galaxies evolve through a dramatic wet-compaction event, which tends to occur at its maximum strength when the galaxy mass is near or above the golden value, $M_v \sim 10^{12} M_\odot$ and $M_s \sim 10^{10} M_\odot$, especially in the redshift range $z = 1-5$ when the gas fraction is high (Zolotov et al. 2015; Tacchella et al. 2016b; Tomassetti et al. 2016). This event is a significant gaseous contraction into a compact central star-forming core within the inner 1 kpc, termed “blue nugget” (BN). The gas consumption by star formation and the associated gas ejection by stellar and supernova feedback lead to central gas depletion and inside-out quenching of star-formation rate (SFR) at a roughly constant central stellar density (Tacchella et al. 2016a). This is illustrated in Fig. 5, a cartoon that represents the evolution seen in many simulated galaxies, showing the evolution of gas mass, stellar mass and SFR within the inner kiloparsec. Figure 6 shows evolution tracks

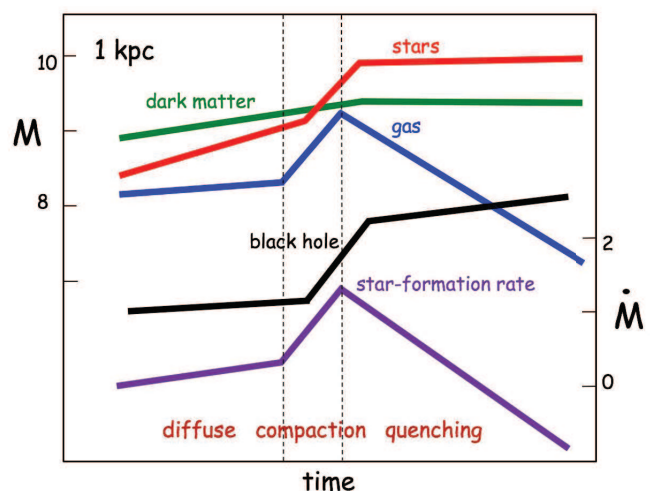


Fig. 5. A cartoon describing a typical wet-compaction event as seen in cosmological simulations, showing the evolution of masses (in $\log(M/M_\odot)$) within the inner 1 kpc (based on Zolotov et al. 2015). The compaction is the steep rise of gas mass (blue), by an order of magnitude during $\sim 0.3 t_{\text{Hubble}}$, reaching a peak as a blue nugget (BN), and soon after declining as the central gas is depleted by star formation and outflows with no replenishment. The SFR (magenta, in $\log(M_\odot \text{ yr}^{-1})$) follows closely, demonstrating post-BN compaction-triggered central quenching. The central stellar mass (red) is rising accordingly during the compaction, and it flattens off post-BN. The inner 1 kpc is dominated by dark matter (green) pre compaction and by baryons (stars, red) post compaction. The “disk” kinematics is dispersion-dominated pre-BN and rotation-dominated post-BN. The time of the major blue-nugget event is typically when the galaxy is near the golden mass, $M_s \sim 10^{10} M_\odot$, separating between the pre-compaction supernova phase and the post-compaction hot-CGM phase. The black-hole growth (black, §6), which is suppressed by supernova feedback pre compaction, is growing during and after the compaction in the hot-CGM phase above the golden mass. The onset of rapid black-hole growth is driven by the compaction event.

of eight galaxies from the VELA zoom-in cosmological simulations (with high spatial resolution of ~ 25 pc in the dense regions) in the plane of specific SFR (sSFR) versus compactness as measured by the stellar surface density within 1 kpc, Σ_1 (Zolotov et al. 2015; Lapiner et al. 2019). A compaction at a roughly constant sSFR turns into a quenching at a constant Σ_1 , generating an L-shape evolution track with the “knee” marking the blue-nugget phase. This characteristic L-shape evolution track has been confirmed observationally (Barro et al. 2017a, Fig. 7).

It became evident that the observed massive, passive galaxies, which are already abundant at $z \sim 2-3$, are compact (or have compact cores), encompassing $\sim 10^{10} M_\odot$ of stars within 1 kpc, termed “red nuggets” (van Dokkum et al. 2008; Damjanov et al. 2009; Newman et al. 2010; van Dokkum et al. 2010; Damjanov et al. 2011; Whitaker et al. 2012; Bruce et al. 2012; van Dokkum et al. 2014, 2015). The effective radii of these compact stellar systems, with respect to their halo virial radii (indicated, e.g., from the universal stellar-to-halo mass relation), are typically of order ~ 0.01 . This is smaller than one would expect had the gas started in the halo with a standard spin of $\lambda \sim 0.035$ and conserved angular momentum during the infall into the central galaxy, thus indicating dissipative inflow associated with angular-momentum loss – a wet compaction (Dekel & Burkert 2014). This implies the presence of blue nuggets as the immediate progenitors of the red nuggets. Indeed, star-forming blue nuggets have been convinc-

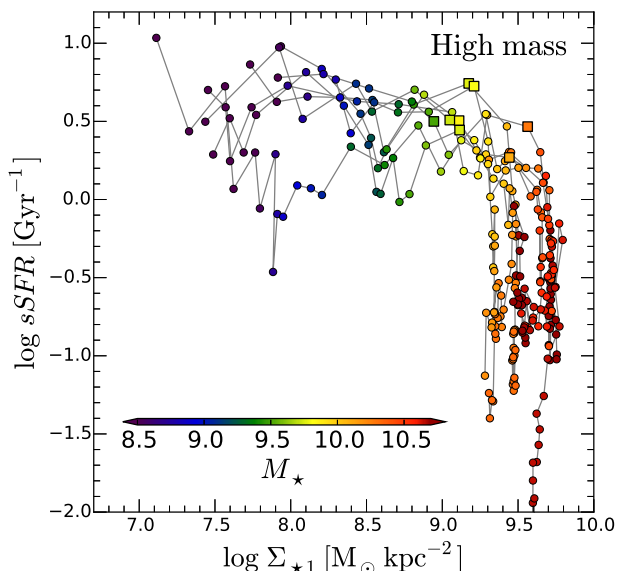


Fig. 6. The universal L-shape evolution track of eight galaxies from the VELA zoom-in cosmological simulations in the plane of sSFR and stellar surface density within 1 kpc, Σ_1 , which serves as a measure of compactness (Dekel et al. 2019, in prep.). The compactness is growing at a roughly constant sSFR (horizontally) before and during the compaction event, turning over at the blue-nugget phase (the “knee”, marked by a square symbol) to quenching at a constant Σ_1 (vertically). A similar behavior is seen observationally (Barro et al. 2017a, Fig. 7), with the value of Σ_1 at the blue-nugget phase weakly increasing with redshift.

ingly observed, with masses, structure, kinematics and abundance consistent with being the progenitors of the red nuggets (Barro et al. 2013, 2014a,b; Williams et al. 2014; Barro et al. 2015; van Dokkum et al. 2015; Williams et al. 2015; Barro et al. 2016b,a, 2017b,a). In particular, a machine-learning study, after being trained on the blue nuggets as identified in the simulations, recognized with high confidence similar blue nuggets in the CANDELS-HST multi-color imaging survey of $z = 1 - 3$ galaxies (Huertas-Company et al. 2018).

The compaction process requires a significant dissipative angular-momentum loss. This is found in the simulations to be caused either by wet mergers ($\sim 40\%$ by major plus minor mergers), by colliding counter-rotating streams, by recycling fountains and by other processes (Dekel et al. 2019, in prep.), and to be possibly associated with violent disk instability (Dekel & Burkert 2014). These processes preferentially occur at high redshifts, where the overall accretion is at a higher rate and more gaseous, leading to deeper compaction events.

The compaction to blue-nugget event marks drastic transitions in the galaxy structural, compositional, kinematic and other physical properties, which translate to pronounced changes as a function of mass near the critical mass (Zolotov et al. 2015; Tacchella et al. 2016a,b). As mentioned, the compaction triggers inside-out quenching of star formation, to be maintained by a hot CGM in massive halos possibly aided by AGN feedback (§5). This is accompanied by a structural transition from a diffuse and largely amorphous configuration to a compact system, possibly surrounded by an extended gas-rich ring and/or a stellar envelope. The kinematics evolves accordingly from pressure to rotation support. Most noticeable is a compaction-driven transition from central dark-matter dominance to baryon dominance, which induces a transition of global shape from a prolate to an oblate stellar system (Tomassetti et al. 2016). Finally, the blue

nugget marks a transition in the central black-hole growth rate from slow to fast (§6), which induces a transition from supernova feedback to AGN feedback as the main source for quenching.

According to the simulations, minor compaction events may occur at all masses in the history of a star-forming galaxy (SFG). Indeed, repeated episodes of compactions and subsequent quenching attempts can explain the confinement of SFGs to a narrow Main Sequence (Tacchella et al. 2016b). However, the major compaction events, those that involve an order-of-magnitude increase in central density, cause a transition from central dark-matter dominance to baryon dominance, and trigger significant quenching, are predicted by the simulations to occur near the golden mass, Tomassetti et al. (2016, Fig. 8) and Zolotov et al. (2015, Fig. 21). This has been confirmed by the deep-learning study of VELA simulations versus observed CANDELS galaxies (Huertas-Company et al. 2018), which detected a preferred stellar mass for the observed blue nuggets near the golden mass, $M_s \sim 10^{10} M_\odot$. The significance of this finding is strengthened by the fact that the same characteristic mass has been recovered after eliminating from the training set the direct information concerning the mass, through the galaxy luminosity.

We argue that the origin of the favored mass for major compaction events is rooted in the two basic processes addresses in §2 and §3, namely the supernova feedback that dominates below the critical mass and the hot CGM that dominates above the critical mass. Central supernova feedback, that is boosted following the SFR soon after the early phases of the compaction process, removes central gas and halts further compaction in galaxies below the critical mass for efficient supernova feedback. Supporting evidence for the effect of supernova feedback on the depth of compaction events is provided by simulations with stronger feedback, which indeed show compaction events that are less dramatic (NIHAO, New Horizon, in prep.). Near and above the critical mass, where the potential well is deep enough and becomes even deeper due to the compaction itself, the compaction is not significantly affected by supernova feedback and it can proceed to higher central densities. Thus, we propose that major compactions tend to occur in galaxies near the critical mass primarily due to the fact that supernova feedback becomes inefficient near and above this mass.

5. Quenching Trigger & Maintenance

In order to understand the evolution within the central 1 kpc of a galaxy, and in particular the quenching process at and above the critical mass, it is helpful to appeal to the key parameter $t_{\text{inf}}/t_{\text{dep}}$, the ratio of timescales for gas inflow into this region and gas depletion from it, by star formation and outflows (Tacchella et al. 2016b). Wet compaction is possible if $t_{\text{inf}} < t_{\text{dep}}$, such that significant dissipative compaction can occur before the gas would turn to stars or be ejected by feedback (Dekel & Burkert 2014). This is also the condition for halting an ongoing depletion-quenching event and starting a new compaction event by newly accreted gas. On the other hand, the condition for quenching is $t_{\text{dep}} < t_{\text{inf}}$, ensuring that significant depletion occurs before the gas may be replenished by accretion.

In the cold-flow regime below the critical mass for virial shock heating (§3), the specific inflow rate into the galaxy roughly follows that of the cosmological total specific accretion rate into the halo. In the EdS regime (roughly $z > 1$) this is derived analytically and confirmed by simulations (Dekel et al. 2013) to be

$$t_{\text{inf}} \sim 25 \text{ Gyr} (1+z)^{-5/2} M_{12}^{0.14}, \quad (6)$$

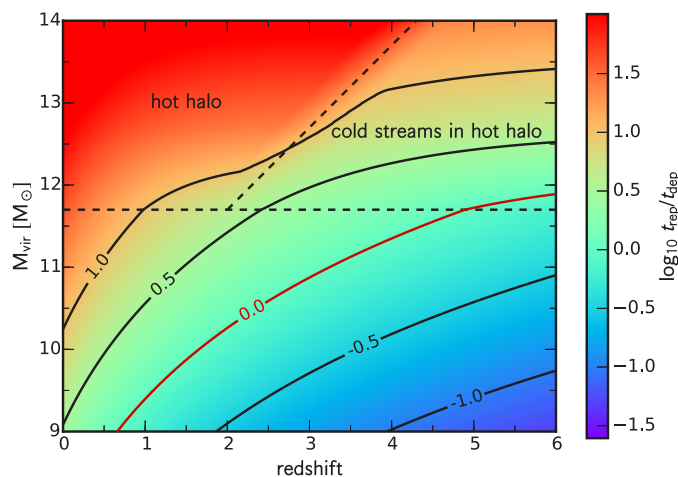


Fig. 7. The ratio of timescales for gas inflow-replenishment and for depletion from the inner 1 kpc, in the halo mass versus redshift plane, distinguishing between necessary conditions for wet compactions and star formation when $t_{\text{inf}}/t_{\text{dep}} < 1$ and deep quenching when $t_{\text{inf}}/t_{\text{dep}} > 1$ (following Tacchella et al. 2016b). Resembling the characteristic masses deduced from Fig. 3, the border line $t_{\text{inf}}/t_{\text{dep}} = 1$ is near the golden mass at $z \leq 2$, rising toward higher redshifts to allow for cold streams, consistent with Fig. 4 derived from observations.

where M_{12} is the halo mass in $10^{12} M_{\odot}$. It implies that below the critical mass t_{inf} is a strong function of redshift and a weak function of mass. The inflow time becomes much longer once the halo is above the critical mass, where the heated CGM suppresses the cold gas supply, and especially at $z < 2$, when the penetration of cold streams through the hot CGM is suppressed (Dekel & Birnboim 2006; Cattaneo et al. 2006).

The average depletion time near the ridge of the Main Sequence of SFGs, as estimated from simulations (Tacchella et al. 2016b) and observations at $z = 1 - 3$ (Tacconi et al. 2018), is approximately

$$t_{\text{dep}} \sim 1 \text{ Gyr} (1+z)^{-0.5} M_{12}^{-0.2}. \quad (7)$$

Here the depletion time is a weak function of both redshift and mass. We thus have below the critical mass

$$\frac{t_{\text{inf}}}{t_{\text{dep}}} \sim 25 (1+z)^{-2} M_{12}^{0.34}. \quad (8)$$

For galaxies of $M_{12} \sim 0.3$, say, we have $t_{\text{inf}} \sim t_{\text{dep}}$ at $z \sim 3$. At higher redshifts it is more likely to have $t_{\text{inf}}/t_{\text{dep}} < 1$, a necessary condition for wet compaction when there is a trigger, followed by a burst of star formation. At lower redshifts, where $t_{\text{inf}}/t_{\text{dep}} > 1$ is more common, there is efficient post-compaction central gas depletion with no efficient replenishment by fresh cold gas, allowing deeper long-term quenching, especially when the CGM is hot above the critical mass.

Figure 7, borrowed from Tacchella et al. (2016b), shows the expected quenching efficiency, the ratio $t_{\text{inf}}/t_{\text{dep}}$, as a function of halo mass and redshift. There is an encouraging qualitative resemblance between this and Fig. 4, which shows in the same plane the distribution of star-forming fraction as estimated from observations via abundance matching.

Overall, the quenching mechanism is primarily a function of mass. In haloes of masses below the critical mass there is quenching by stellar and supernova feedback. Especially at high redshift, cold gas supply may cause a new compaction event and a new burst of star formation, with boosted supernova feedback

that triggers a new quenching attempt. The associated oscillations of $t_{\text{inf}}/t_{\text{dep}}$ about unity cause oscillations about the Main Sequence of SFGs, which can explain the confinement of SFGs to a narrow Main Sequence (Tacchella et al. 2016b). Near the critical mass, a major compaction event triggers a central burst of star formation, which leads to the onset of deeper quenching by gas consumption and supernova feedback that is not followed by efficient replenishment. The triggered quenching is maintained in haloes above the critical mass because the hot CGM suppresses gas supply to the central galaxy. This is especially efficient at low redshifts ($z < 2$), where cold streams do not bring gas in above the critical mass (Dekel & Birnboim 2006). As discussed below, in the hot-CGM regime, a major compaction event also activates a rapid growth of the central black hole, leading to AGN that helps keeping the CGM hot and thus maintain the quenching of star formation.

6. Black Hole Growth

The evolution of galaxies from the supernova zone below the critical mass, through a compaction event near the critical mass, into the hot-CGM phase above the critical mass, determines the black-hole growth rate and imprints the golden mass in it. Below the critical mass, namely pre-compaction, the supernova-driven gas heating and ejection from the center suppresses the black-hole growth. The major compaction that tends to occur near the critical mass, where supernova feedback is already inefficient, brings gas into the inner sub-kiloparsec blue nugget. This can induce efficient accretion onto the sub-parsec black hole, which can trigger rapid black-hole growth and the activation of an AGN. In more massive haloes the deep potential well and the hot CGM lock the central gas in, and allow continuing accretion onto the black hole.

The suppression of black-hole growth by supernova feedback below the critical mass and the transition to rapid black-hole growth above it have been demonstrated in several different cosmological simulations, which were run with and without supernova feedback. This phenomenon is robust given that the simulations have been using different codes and subgrid recipes and especially different implementations of supernova feedback and black-hole growth. It was first seen in a RAMSES simulation by Dubois et al. (2015) and Habouzit et al. (2017), and then in EAGLE simulations (Bower et al. 2017), FIRE simulations (Anglés-Alcázar et al. 2017) and Illustris TNG (Habouzit et al. 2018).

This phenomenon, and in particular the crucial role of wet compaction in triggering the black-hole growth near the golden mass, is demonstrated in ten massive galaxies from the New-Horizon cosmological simulation (Dubois et al. in prep.). We summarize here the preliminary results, to be analyzed in more detail in (Lapiner et al. 2019).

Figure 8 (left panel) shows the evolution of black-hole mass (scaled) and the masses of gas and stars within the inner 1 kpc as a function of expansion factor $a = (1+z)^{-1}$ in a New-Horizon simulated galaxy. The gas (blue) shows a wet-compaction event, with an onset at $a \simeq 0.21$ and a blue-nugget peak at $a \simeq 0.26$. The history of SFR within the inner 1 kpc (not shown) follows closely the gas history. The associated stellar mass within 1 kpc (red) is rising until the blue-nugget peak and flattens off thereafter. The total stellar mass (dashed red) at the blue-nugget peak is $\simeq 10^{10.15} M_{\odot}$, representing the golden stellar mass scale. We see a suppressed black-hole growth in the pre-compaction supernova regime and a rapid growth post compaction. The black-

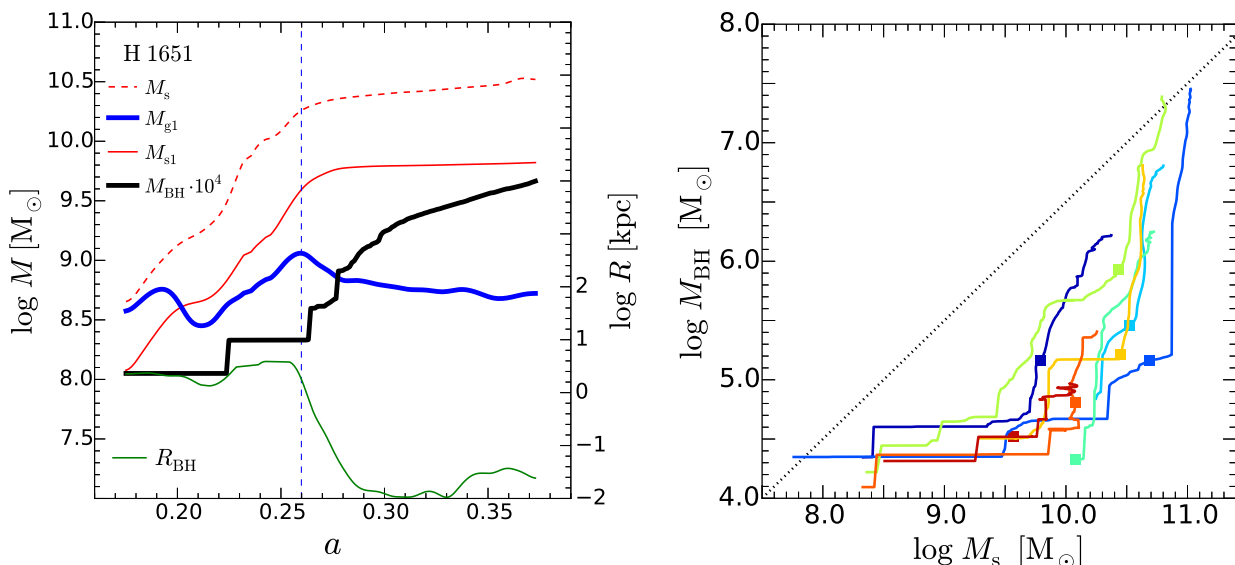


Fig. 8. Compaction-driven black-hole growth in New-Horizon simulations (Lapiner et al. 2019). **Left:** Evolution of black-hole mass ($\times 10^4$, black) and gas mass within 1 kpc (blue) as a function of cosmological expansion factor a in a simulated galaxy. The black-hole growth is suppressed by supernova feedback at early times. The compaction event, marked by the rise of the gas mass to a peak, triggers a rapid black-hole growth. The galaxy stellar mass (dashed red) at that time is near the critical mass $\sim 10^{10.3} M_\odot$. The compaction brings the black hole to the galaxy center (green, $\log R$). **Right:** Evolution tracks of black-hole mass versus stellar mass M_s in eight galaxies. They show supernova-driven suppression of black-hole growth below a critical mass of $M_s \sim 10^{10} M_\odot$, turning into a rapid growth near the critical mass, likely driven by compaction events (squares). Similar L-shape tracks are seen when M_{bh} is plotted against bulge mass or Σ_1 . Black holes of $\sim 10^5 M_\odot$ are thus predicted to lie below the standard linear relation.

hole growth starts at the onset of compaction, and it continues throughout the compaction process and later on into the hot-CGM regime.

Figure 8 (right panel) puts together eight simulated galaxies, showing the evolution tracks of black-hole mass versus total stellar mass M_s . A characteristic L-shape evolution is seen, displaying a suppression of black-hole growth below the golden mass of $M_s \sim 10^{10} M_\odot$ and a rapid black-hole growth once above the golden mass. The blue-nugget phase, marked by a square symbol, typically coincides with the upturn of the curve, consistent with a causal connection between the two. This is also demonstrated when M_{bh} is plotted against Σ_1 , the stellar surface density within the inner 1 kpc, which serves as a measure of compactness as in Fig. 6. A similar turnover is found to occur at a characteristic threshold of $\Sigma_1 \sim 10^9 M_\odot \text{kpc}^{-2}$, consistent with compaction-driven black-hole growth. Similar tracks are seen when M_{bh} is plotted against the bulge mass, predicting that black holes of $\sim 10^5 M_\odot$ should lie well below the standard linear relation between black-hole mass and bulge mass that has been established for black holes more massive than $10^6 M_\odot$ (Magorrian et al. 1998; Kormendy & Ho 2013).

A clue for how the compaction triggers the black-hole growth is provided by tracing the position of the black hole with respect to the galaxy center. The green curve in Fig. 8 shows that during the pre-compaction phase the black hole orbits at a few kiloparsecs off the center, where the orbital velocity and the supernova-driven dilute-gas environment suppresses the accretion onto the black hole. Soon after the compaction, the black hole sinks to the ~ 10 pc vicinity of the galaxy center, due to drag against the compaction-driven dense gas and deep potential well once above the golden mass. Once at rest in the dense galaxy center, the black hole is subject to efficient accretion. The wondering of the black holes off the centers has been also seen in simulations of low-mass galaxies by Bellovary et al. (2019).

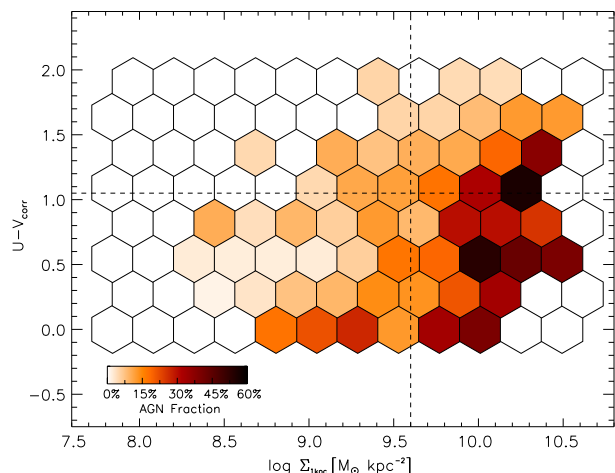


Fig. 9. Fraction of CANDELS galaxies that host AGN (color scale) in the plane of SFR (growing downwards) and compactness, as represented by U-V color and stellar surface density inside 1 kpc $\Sigma_{1 \text{ kpc}}$ respectively (following Kocevski et al. 2017, where the effective radius was used). The AGN fraction is high in the blue-nugget quadrant of compact star-forming galaxies (bottom-right), consistent by compaction-driven compaction.

Figure 9, similar to Kocevski et al. (2017), shows the fraction of CANDELS-survey galaxies that host AGN in the plane of SFR versus compactness, as measured by U-V color and stellar surface brightness within 1 kpc, Σ_1 , respectively. This plane is similar to the plane shown in Fig. 6, where the L-shape evolution tracks are detected, except that the SFR is growing downwards. One can indeed see a high AGN fraction in the quadrant of high SFR and high compactness representing the blue nugget phase of evolution, as predicted. Similar evidence comes from

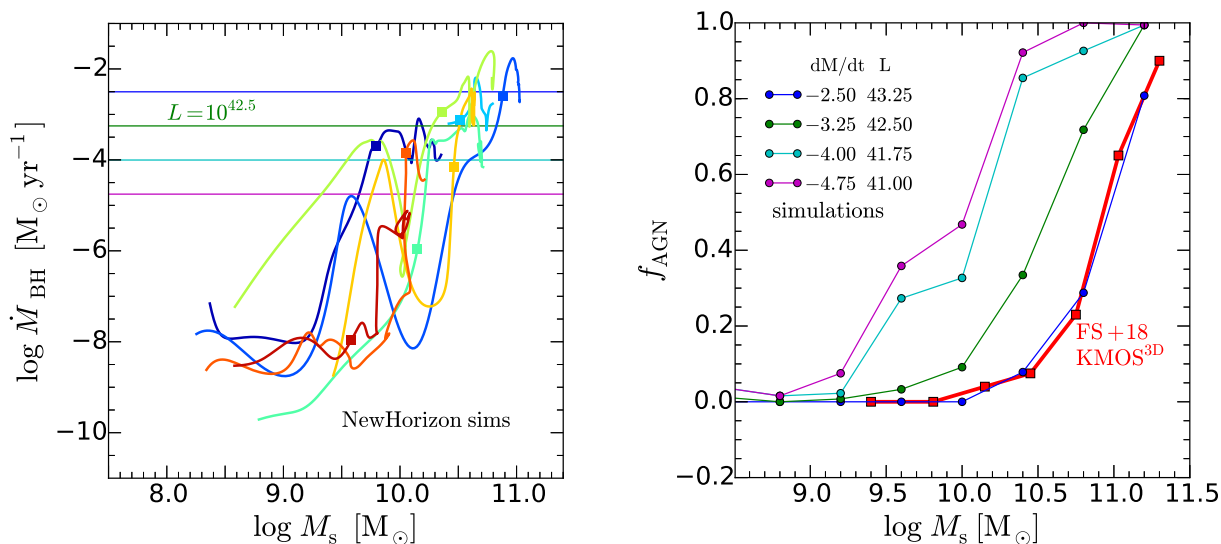


Fig. 10. **Left:** Accretion rate onto the black hole versus M_s in New-Horizon simulations (Lapiner et al. 2019), showing L-shape tracks with a turnover near the golden mass, similar to Fig. 8 (right). **Right:** When AGN are selected above a threshold luminosity (lines in the left panel with $L = 0.1 \dot{M}_{\text{BH}}/dt c^2$), the fraction of galaxies that host AGN is plotted versus M_s . A threshold in the range $10^{42.5-43.25} \text{ erg s}^{-1}$ (green-blue) seems to match the observed AGN fractions (red curve, Förster Schreiber et al. 2018).

obscured AGN that tend to reside in compact star-forming galaxies (Chang et al. 2017).

In order to reproduce the fraction of galaxies that host AGN as a function of their stellar mass based on the New-Horizon simulations, we plot in the left panel of Fig. 10 the accretion rates onto the black hole as a function of M_s for the eight massive galaxies. By assuming an AGN luminosity of $L = 0.1 dM_{\text{bh}}/dt c^2$, one can apply a luminosity threshold to select AGN for a sample. The resultant AGN fraction, for each given threshold, is shown in the right panel of Fig. 10, in comparison to the fraction observed by Förster Schreiber et al. (2018) using an effective luminosity threshold of $10^{42.5} \text{ erg s}^{-1}$ (red curve). The predicted curves all resemble in their general shape the observed curve, though the turnover mass is shifted as a function of the luminosity threshold. When assuming the same threshold as in the observed sample (green), the turnover mass is apparently underestimated by 0.4dex, while a threshold of $10^{43.25} \text{ erg s}^{-1}$ (blue) provides a perfect fit. It is not clear whether this offset reflects an uncertainty in the luminosity threshold applied in the observations and its correspondence to accretion rate or a real underestimate of the golden mass in the simulations. We should note that while the existence of a golden mass is robust, rooted in the physical phenomena discussed above, the exact value of the golden mass in each simulation may be subject to the way the subgrid physics of supernova feedback and black-hole growth are implemented.

Förster Schreiber et al. (2018) also provide in their figure 9 an indication for an anti-correlation between the AGN fraction and the stellar effective radius for galaxies of $M_s \sim 10^{10.00-10.75} \text{ M}_{\odot}$, consistent with the predicted compaction-driven AGN activity at and above the golden mass. Their figure 3 indicates a correlation of AGN fraction with ΔMS , the deviation from the ridge of the Main Sequence of star-forming galaxies at a given stellar mass, consistent with the onset of AGN activity at the blue-nugget phase, where the galaxy is above the Main-Sequence ridge (Tacchella et al. 2016b), similar to what is seen in Fig. 9.

7. Conclusion

Observations reveal a golden mass scale for efficient star formation in galaxies within dark-matter halos, at $M_v \sim 10^{12} \text{ M}_{\odot}$. We point out that this translates to the golden time for star formation at $z \sim 2$ because the (Press-Schechter) mass of typical forming halos at that epoch is comparable to the golden mass. The apparent threshold for luminous AGN at a similar mass, while there is no hint in black-hole physics for a characteristic mass of this sort, indicates that it is imprinted on the central black hole by processes associated with galaxy evolution.

Two physical processes confine the golden mass. On the low-mass side, energetic considerations imply that supernova feedback is effective in suppressing star formation for $M < M_{\text{crit}}$ (e.g. Dekel & Silk 1986). On the high-mass side, an analysis of virial shock stability reveals that the halo CGM is heated to the virial temperature for $M > M_{\text{crit}}$ (e.g. Dekel & Birnboim 2006). The resemblance of the critical masses associated with these two different processes (Fig. 3) confines efficient galaxy formation to a peak about the golden mass. One may wonder whether this similarity between the two critical masses is a coincidence or a built-in match. On one hand, the analyses in the two cases are related in the sense that the preferred scale arises from comparing a radiative cooling time to the relevant dynamical time. On the other hand, these timescales refer to different environments on different scales. The conditions for cooling (e.g., gas density and metallicity) and the relevant dynamical times (in star-forming clouds versus at inflow into the halo) are very different.

Cosmological simulations (Zolotov et al. 2015) and observations (Barro et al. 2013, 2017a) reveal that most galaxies undergo wet-compaction events throughout their histories, events that induce major transitions in the galaxy properties. In particular, the compactions trigger quenching of star formation by central gas depletion, to star formation and outflows. The compaction processes are due to drastic angular-momentum losses, about 40% caused by mergers and the rest by counter-rotating streams, recycling fountains and other mechanisms. The major deep compaction events to blue nuggets, those that trigger a decisive long-term quenching process and a transition from central

dark-matter to baryon dominance, tend to occur near the golden mass, at all redshifts. This is seen in simulations (Zolotov et al. 2015; Tomassetti et al. 2016) and in machine-learning-aided comparisons to observations (Huertas-Company et al. 2018). We argue that this preferred mass scale for major compactions is due to the same two physical processes of supernova feedback and hot CGM, which tend to suppress compaction attempts at lower and higher masses.

We argue that the characteristic threshold mass for rapid black-hole growth and AGN reflects the golden mass of galaxy formation. Black-hole growth is suppressed by supernova feedback in star-forming galaxies of mass below the golden mass, pre-compactation. Black holes can grow above the golden mass as the gas is confined to the center by the halo potential well and hot CGM. In between the supernova and CGM phases, the onset of rapid black growth is driven by the major compaction event, near the golden mass.

The quenching of star formation at $M > M_{\text{crit}}$ is thus a multi-stage process. It is triggered by a major compaction event, via central gas depletion due to star formation and the associated outflows. The quenching is then maintained by the hot CGM that suppresses the cold gas supply in $M > M_{\text{crit}}$ halos, especially at $z < 2$ when cold streams hardly penetrate the hot CGM. Finally, AGN feedback, triggered by the compaction-driven black-hole growth, helps keeping the CGM hot and maintaining long-term quenching. Note that in this advocated scenario, contrary to a common belief, AGN feedback is not responsible for the onset of quenching. Instead, they both result from the same wet compaction event once the galaxy is near the golden mass. AGN feedback kicks in later on as a source of quenching maintenance. In other words, AGN feedback is not responsible for the golden mass and epoch for galaxy formation, but it helps emphasizing it by further heating the gas post compaction while in the hot CGM zone and after departing the SN zone.

It may be interesting to consider the interplay between the galaxy on large scales and its central region during the different phases. In the star-forming supernova regime below the golden mass, cold flows that originate from outside the halo induce star formation that is regulated by supernova feedback, which suppresses the central black-hole growth. Near the golden mass, major compaction events that are induced externally by mergers and counter-rotating streams form compact star-forming blue nuggets, which trigger central quenching inside out. The compaction outside-in causes a rapid central black-hole growth. Above the golden mass, the hot CGM maintains the quenching by suppressing the cold gas supply from the halo to the center. The halo deep potential well and hot CGM lock the supernova ejecta at the galaxy center and allow a continuous black-hole growth. The resultant central AGN helps the quenching on larger scales by keeping the CGM hot. There is thus a strong two-way cross-talk between the galaxy at large, its dark matter halo and the cosmic web, and the galactic center with its supermassive black hole.

References

Anglés-Alcázar, D., Faucher-Giguère, C.-A., Quataert, E., et al. 2017, *MNRAS*, 472, L109
 Barro, G., Faber, S. M., Dekel, A., et al. 2016a, *ApJ*, 820, 120
 Barro, G., Faber, S. M., Koo, D. C., et al. 2017a, *ApJ*, 840, 47
 Barro, G., Faber, S. M., Perez-Gonzalez, P. G., et al. 2013, *ApJ*, 765, 104
 Barro, G., Faber, S. M., Perez-Gonzalez, P. G., et al. 2014a, *ApJ*, 791, 52
 Barro, G., Kriek, M., Pérez-González, P. G., et al. 2017b, *ApJ*, 851, L40
 Barro, G., Kriek, M., Pérez-González, P. G., et al. 2016b, *ApJ*, 827, L32

Barro, G., Trump, J., Koo, D. C., et al. 2015, in *American Astronomical Society Meeting Abstracts*, Vol. 225, American Astronomical Society Meeting Abstracts, 111.07
 Barro, G., Trump, J. R., Koo, D. C., et al. 2014b, arXiv:1405.7042
 Behroozi, P. 2016, in *Santa Cruz Workshop on Galaxy Formation* <http://hipacc.ucsc.edu/GalaxyWorkshop2016.html>, 1
 Behroozi, P., Wechsler, R., Hearin, A., & Conroy, C. 2018, arXiv e-prints [1806.07893]
 Behroozi, P. S., Wechsler, R. H., & Conroy, C. 2013, *ApJ*, 762, L31
 Bellovary, J. M., Cleary, C. E., Munshi, F., et al. 2019, *MNRAS*, 482, 2913
 Binney, J. 1977, *ApJ*, 215, 483
 Birnboim, Y. & Dekel, A. 2003, *MNRAS*, 345, 349
 Bouché, N., Dekel, A., Genzel, R., et al. 2010, *ApJ*, 718, 1001
 Bower, R. G., Schaye, J., Frenk, C. S., et al. 2017, *MNRAS*, 465, 32
 Bruce, V. A., Dunlop, J. S., Cirasuolo, M., et al. 2012, *MNRAS*, 427
 Cattaneo, A., Dekel, A., Devriendt, J., Guiderdoni, B., & Blaizot, J. 2006, *MNRAS*, 370, 1651
 Cattaneo, A. & Teyssier, R. 2007, *MNRAS*, 376, 1547
 Chang, Y.-Y., Le Floch, E., Juneau, S., et al. 2017, *MNRAS*, 466, L103
 Croton, D. J., Springel, V., White, S. D. M., et al. 2006, *MNRAS*, 365, 11
 Damjanov, I., Abraham, R. G., Glazebrook, K., et al. 2011, *ApJ*, 739, L44
 Damjanov, I., McCarthy, P. J., Abraham, R. G., et al. 2009, *ApJ*, 695, 101
 Dekel, A. & Birnboim, Y. 2006, *MNRAS*, 368, 2
 Dekel, A. & Birnboim, Y. 2008, *MNRAS*, 383, 119
 Dekel, A. & Burkert, A. 2014, *MNRAS*, 438, 1870
 Dekel, A., Sarkar, K. C., Jiang, F., et al. 2019, arXiv e-prints [1903.00962]
 Dekel, A. & Silk, J. 1986, *ApJ*, 303, 39
 Dekel, A. & Woo, J. 2003, *MNRAS*, 344, 1131
 Dekel, A., Zolotov, A., Tweed, D., et al. 2013, *MNRAS*, 435, 999
 Di Cintio, A., Brook, C. B., Dutton, A. A., et al. 2017, *MNRAS*, 466, L1
 Dubois, Y., Devriendt, J., Teyssier, R., & Slyz, A. 2011, *MNRAS*, 417, 1853
 Dubois, Y., Volonteri, M., Silk, J., et al. 2015, *MNRAS*, 452, 1502
 Dutton, A. A., Macciò, A. V., Dekel, A., et al. 2016, *MNRAS*, 461, 2658
 Förster Schreiber, N. M., Übler, H., Davies, R. L., et al. 2018, arXiv e-prints [1807.04738]
 freundlich, J., Dekel, A., Jiang, F., et al. 2019, arXiv:1900.0000
 Garrison-Kimmel, S., Rocha, M., Boylan-Kolchin, M., Bullock, J. S., & Lally, J. 2013, *MNRAS*, 433, 3539
 Habouzit, M., Genel, S., Somerville, R. S., et al. 2018, arXiv e-prints [1809.05588]
 Habouzit, M., Volonteri, M., & Dubois, Y. 2017, *MNRAS*, 468, 3935
 Huertas-Company, M., Primack, J. R., Dekel, A., et al. 2018, *ApJ*, 858, 114
 Jiang, F., Dekel, A., Freundlich, J., et al. 2018, arXiv e-prints [1811.10607]
 Kauffmann, G., Heckman, T. M., Tremonti, C., et al. 2003, *MNRAS*, 346, 1055
 Kereš, D., Katz, N., Weinberg, D. H., & Davé, R. 2005, *MNRAS*, 363, 2
 Koccevski, D. D., Barro, G., Faber, S. M., et al. 2017, *ApJ*, 846, 112
 Kormendy, J. & Ho, L. C. 2013, *ARA&A*, 51, 511
 Lapiner, S., Dekel, A., Dubois, Y., et al. 2019, arXiv:1900.0000
 Madau, P. & Dickinson, M. 2014, *ARA&A*, 52, 415
 Magorrian, J., Tremaine, S., Richstone, D., et al. 1998, *AJ*, 115, 2285
 Moster, B. P., Somerville, R. S., Maubetsch, C., et al. 2010, *ApJ*, 710, 903
 Nelson, D., Genel, S., Pillepich, A., et al. 2016, *MNRAS*, 460, 2881
 Nelson, D., Vogelsberger, M., Genel, S., et al. 2013, *MNRAS*, 429, 3353
 Newman, A. B., Ellis, R. S., Treu, T., & Bundy, K. 2010, *ApJ*, 717, L103
 Oevirk, P., Pichon, C., & Teyssier, R. 2008, *MNRAS*, 390, 1326
 Ostriker, E. C. & Shetty, R. 2011, *ApJ*, 731, 41
 Pontzen, A. & Governato, F. 2012, *MNRAS*, 421, 3464
 Press, W. H. & Schechter, P. 1974, *ApJ*, 187, 425
 Rees, M. J. & Ostriker, J. P. 1977, *MNRAS*, 179, 541
 Reines, A. E. & Volonteri, M. 2015, *ApJ*, 813, 82
 Silk, J. 1977, *ApJ*, 211, 638
 Silk, J. 1997, *ApJ*, 481, 703
 Tacchella, S., Dekel, A., Carollo, C. M., et al. 2016a, *MNRAS*, 458, 242
 Tacchella, S., Dekel, A., Carollo, C. M., et al. 2016b, *MNRAS*, 457, 2790
 Tacconi, L. J., Genzel, R., Saintonge, A., et al. 2018, *ApJ*, 853, 179
 Tomassetti, M., Dekel, A., Mandelker, N., et al. 2016, *MNRAS*, 458, 4477
 van Dokkum, P. G., Bezanson, R., van der Wel, A., et al. 2014, *ApJ*, 791, 45
 van Dokkum, P. G., Franx, M., Kriek, M., et al. 2008, *ApJ*, 677, L5
 van Dokkum, P. G., Nelson, E. J., Franx, M., et al. 2015, *ApJ*, 813, 23
 van Dokkum, P. G., Whitaker, K. E., Brammer, G., et al. 2010, *ApJ*, 709, 1018
 Vitale, M., Mignoli, M., Cimatti, A., et al. 2013, *A&A*, 556, A11
 Whitaker, K. E., Kriek, M., van Dokkum, P. G., et al. 2012, *ApJ*, 745, 179
 Williams, C. C., Gialalisco, M., Cassata, P., et al. 2014, *ApJ*, 780, 1
 Williams, C. C., Gialalisco, M., Lee, B., et al. 2015, *ApJ*, 800, 21
 Zolotov, A., Brooks, A. M., Willman, B., et al. 2012, *ApJ*, 761, 71
 Zolotov, A., Dekel, A., Mandelker, N., et al. 2015, *MNRAS*, 450, 2327